Energy & Environmental Science

Accepted Manuscript

This article can be cited before page numbers have been issued, to do this please use: R. Tang, C. Sun, J. Yang, S. Li, W. meng, M. Zhang, G. Chen, J. Zhao and Y. Yang, *Energy Environ. Sci.*, 2025, DOI: 10.1039/D5EE01691F.

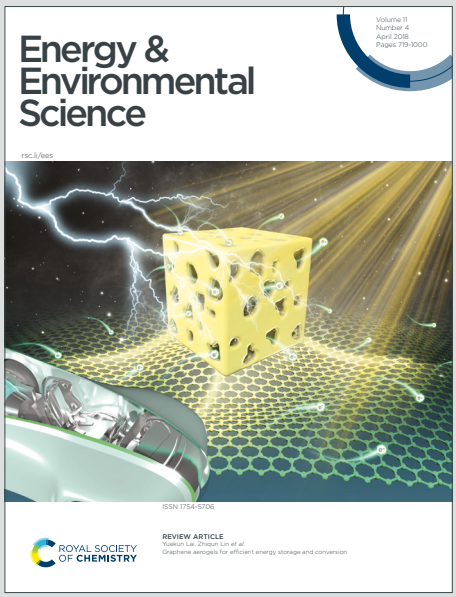

ROYAL SOCIETY OF CHEMISTRY

rsc.li/ees

View Article Online
DOI: 10.1039/D5EE01691F

Broader context

Aqueous Zn−iodine (Zn-I_2) batteries have attracted significant attention due to their high cost-effectiveness, intrinsic safety, and high energy density. However, their practical implementation is impeded by challenges such as the shuttle effect and sluggish iodine redox kinetics. Functionalizing carbon-based hosts with catalytic sites is a widely explored strategy to enhance polyiodide adsorption and catalyze iodine conversion. However, SACs are prone to aggregation over extended cycles, compromising stability, and their synthesis process often involves complex and time-consuming precursor steps, which hinders large-scale production. Meanwhile, nanoparticle electrocatalysts generally exhibit better structural stability but suffer from insufficient catalytic activity for polyiodide conversion, resulting in relatively low iodine utilization and unsatisfactory areal capacity. In this work, Fe-Ni@ACC prepared by Joule heating ultrafast high-temperature (UHT) treatment technology is aimed at overcoming the shuttle polyiodide effect and enhancing the redox kinetics in zinc-iodide batteries. These Fe-Ni alloy nanoparticles are embedded and encapsulated within the nanoholes, just like lotus seeds wrapped in lotus pods. This kind of reaction cavity resembling lotus seed pods provides strong binding interactions, facilitating efficient electron transfer between the nanoparticle catalyst and the carbon matrix, and effectively accommodating iodine species diffusing from the electrode to the bulk electrolyte.

View Article Online
DOI: 10.1039/D5EE01691F

ARTICLE

Lotus seedpod-inspired electrocatalytic interlayer synthesized via ultrafast Joule heat treatment: overcoming polyiodide shuttle and enhancing redox kinetics in high-areal-capacity aqueous zinc-iodine batteries

Received 00th January 20xx,
Accepted 00th January 20xx

DOI: 10.1039/x0xx00000x

Rong Tang,[a] Chenxi Sun,[a] Jin Yang,[a] Siyang Li,[a] Weiwei Meng,[b] Minghao Zhang,[a] Guanhong Chen,[a] Jinbao Zhao, *[a] and Yang Yang*[a]

Aqueous zinc-iodine (Zn-I_2) batteries are gaining attention as cost-effective and safe energy storage solutions with high energy density. However, their practical performance is hindered by issues such as polyiodide dissolution, the shuttle effect, and slow iodine redox kinetics, which restrict reversible areal capacity and cycling stability. Herein, we develop a biomimetic electrocatalytic interlayer (Fe-Ni@ACC) for advanced Zn-I_2 batteries using Joule heat ultrafast high-temperature (UHT) treatment. This bio-inspired structure resembles a lotus seedpod, where ultrafine Fe-Ni alloy nanoparticles (lotus seed) are embedded within activated carbon fibers (lotus seedpod), ensuring strong binding strength and efficient electron transfer. Additionally, the UHT process also induces the spontaneous formation of abundant nanocavities, effectively accommodating iodine species. Comprehensive in situ characterizations and theoretical calculations demonstrate that Fe-Ni alloy nanoparticles, with the unique electronic structure inside nanocavities, significantly accelerates polyiodide conversion through efficient d-p orbital hybridization. Consequently, these lotus seedpod-like reaction chambers effectively anchor polyiodide and enhance iodine redox kinetics, enabling Zn-I_2 batteries to achieve a high areal capacity of 4.05 mAh cm^{-2} and an ultralong lifespan exceeding 12,000 cycles. This work provides a facile and scalable methodological platform for synthesizing electrocatalytic interlayers, advancing the practical implementation of Zn-I_2 batteries.

Introduction

Aqueous zinc-ion batteries (AZIBs) have attracted considerable interest as a cost-effective, eco-friendly, and non-flammable energy storage solution, positioning them as a strong candidate to replace lithium-ion batteries in stationary applications.[1] Unlike conventional AZIBs, which utilizes transition metal oxides[2–4] or organic compounds[5–7] as cathodes, Zn-I_2 batteries stand out owing to their relatively high theoretical capacity (211 mAh g^{-1}),[8] abundant iodine resources,[9] and a high operating potential (1.38 V vs. Zn^{2+}/Zn).[10] However, two critical challenges hinder the development of high-performance I_2 cathodes: low electronic conductivity and polyiodide shuttle effect.[11] The intrinsically poor electronic conductivity of I_2 (~7.6×10^{-8} S cm^{-1}) limits its reaction kinetics, making it difficult to achieve high-areal-capacity electrodes.[12] Additionally, the polyiodide intermediate species (I_3^- and I_5^-) formed during cycling exhibit highly solubility in aqueous electrolytes, resulting in the shuttle effects that corrode Zn metal anodes and cause irreversible capacity loss.[13]

To address these challenges, various strategies have been explored, including host confinement, Zn anode interface protection, electrolyte modification and separator design.[14] Dispersing I_2 into carbon hosts to form composite materials is a straightforward approach to enhancing electronic conductivity and thermal stability.[15–17] However, the weak physical adsorption of non-polar carbon hosts provides only limited binding to polar polyiodides, which is insufficient to suppress the shuttling effect.[18–20] Therefore, carbon-based materials are often functionalized with catalytic sites that offer stronger chemical anchoring interactions, enabling efficient polyiodide adsorption and catalytic conversion of iodine species.[21,22] Typically, single metal atomic catalysts (SACs) on carbon supports, known for their nearly 100% atomic utilization, have been extensively studied to overcome the limitations of traditional carbon hosts and enhance electrochemical performance.[23,24] In 2022, Zhang et al. pioneered a study demonstrating that Fe-SACs embedded in porous carbon could catalyze the iodine redox conversion through the physicochemical confinement effect.[25] More recently, SACs incorporating Ni, Cu, Co, Zn, Nb have also been investigated for accelerating polyiodide conversion.[26–32] Despite their high catalytic activity, SACs are prone to aggregation over extended

[a] State Key Laboratory of Physical Chemistry of Solid Surfaces, State-Province Joint Engineering Laboratory of Power Source Technology for New Energy Vehicle, College of Chemistry and Chemical Engineering, Xiamen University, Xiamen, 361005, P.R. China. E-mail: jbzhao@xmu.edu.cn; yangyang419@xmu.edu.cn.
[b] Key Laboratory of Functional Materials and Devices for Special Environments of CAS, Xinjiang Key Laboratory of Electronic Information Materials and Devices; Xinjiang Technical Institute of Physics & Chemistry of CAS, Urumqi, 830011, P.R. China

† Supplementary Information available: [SEM, XPS, electrochemical tests and calculation results]. See DOI: 10.1039/x0xx00000x

View Article Online
DOI: 10.1039/D5EE01691E

cycles, compromising stability, particularly under high-mass-loading conditions. Additionally, SAC synthesis often involves complex and time-consuming precursor steps, posing difficulties for large-scale production.[33]

Drawing insights from the well-established electrocatalyst design in HER (hydrogen evolution reaction) and ORR (oxygen reduction reaction), it can be inferred that nanoparticle-based electrocatalysts generally exhibit superior structural stability compared to SACs.[34] Accordingly, various nanoparticle electrocatalysts on carbon hosts, such as Co nanoparticles embedded in porous active carbon,[35] carbonized filter paper with high-entropy oxide,[36] and Ni nanoparticles decorated on biomass carbon[37] have been developed to advance Zn-I_2 batteries. However, the catalytic activity of nanoparticle electrocatalysts toward polyiodide conversion remains insufficient, leading to limited I_2 utilization and suboptimal areal capacity (<1 mAh cm^{-2}). From a fundamental perspective, achieving high I_2 utilization requires the synergistic confinement of all iodine species (I_2, I^-, I_3^- and I_5^-), each exhibiting different binding preferences. While metallic sites provide strong binding interactions with polar polyiodides, the adsorption of non-polar I_2 relies on the presence of an optimized pore structure within the carbon host.[38] Therefore, integrating highly active catalytic nanoparticles with a well-developed porous framework through a scalable preparation method presents an effective strategy for realizing practical high-areal-capacity Zn-I_2 batteries.

In this work, we employ Joule heating ultrafast high-temperature (UHT) treatment technology to rapidly fabricate a biomimetic carbon-based host with Fe-Ni alloy nanoparticles encapsulated in activated carbon cloth (Fe-Ni@ACC), which can serve as a powerful interlayer to enable stable and reversible high-areal-capacity Zn-I_2 batteries (Figure 1a).

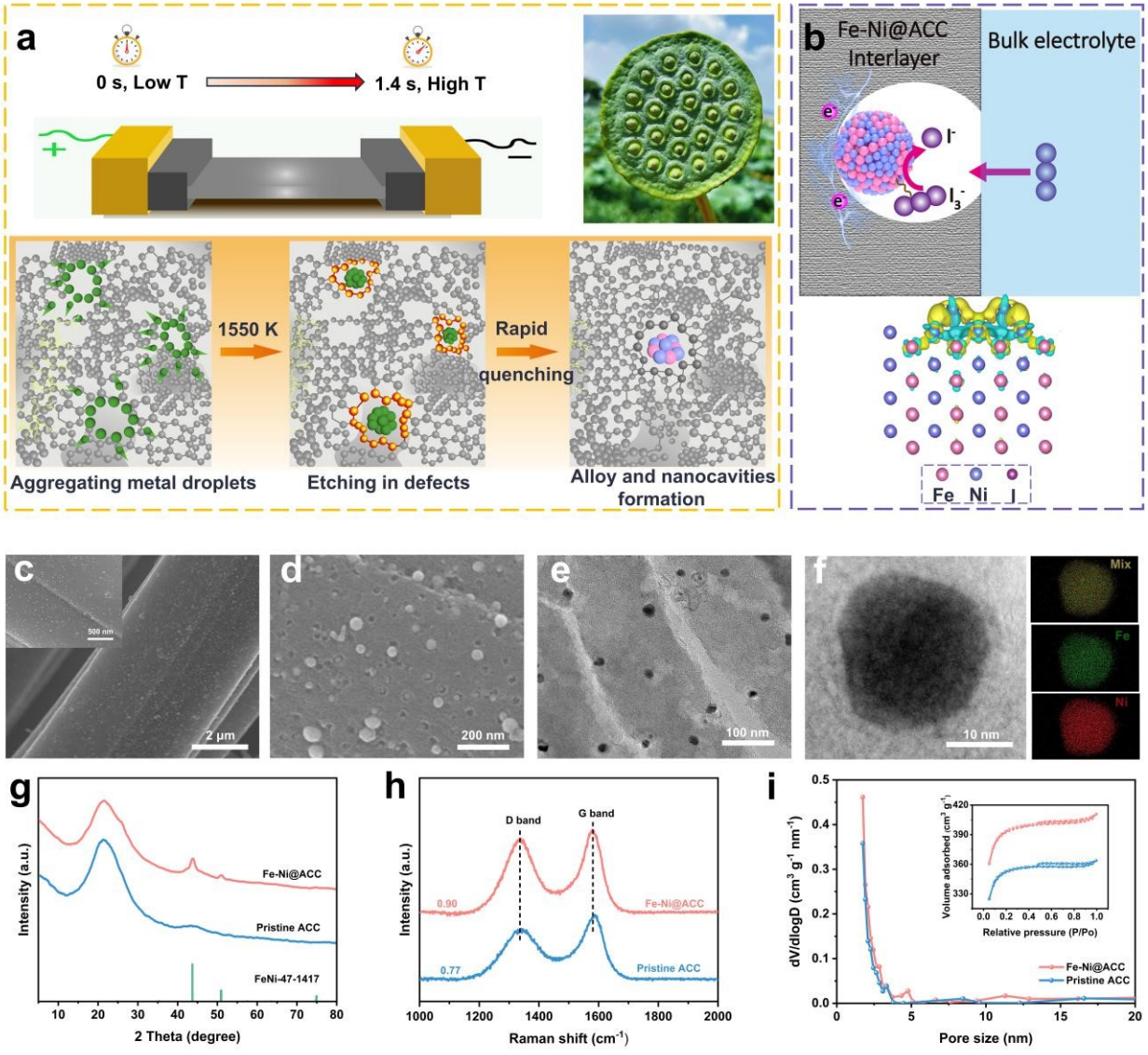

Fig. 1 (a) Schematic for the synthesis of Fe-Ni@ACC through the UHT treatment and rapid quenching treatment. (b) Biomimetic concept of the Fe-Ni@ACC. (c, d) SEM and (e) TEM images of Fe-Ni@ACC. (f) Elemental mapping results of Fe-Ni@ACC. (g) XRD profiles, (h) Raman spectra, and (i) N_2 adsorption-desorption curves of Fe-Ni@ACC and pristine ACC.

View Article Online
DOI: 10.1039/D5EE01691F

This bio-inspired structure resembles a lotus seedpod, where Fe-Ni alloy nanoparticles (lotus seed) are rooted and encapsulated within activated carbon fibers (lotus seedpod), ensuring strong binding strength and efficient electron transfer between nanoparticle catalysts and carbon host. Notably, UHT treatment not only facilitates the uniform dispersion of Fe-Ni alloy nanoparticles but also induces the formation of abundant nanocavities through a spontaneous high-temperature etching effect. These lotus seedpod-like reaction chambers can effectively accommodate iodine species diffusing from the electrode to the bulk electrolyte (Figure 1b). Furthermore, the unique electronic structure of Fe-Ni alloy enhances d-p orbital hybridization with iodine p orbitals, significantly improving reaction kinetics compared to single-component Fe or Ni nanoparticles. Consequently, Zn-I_2 batteries incorporating with the Fe-Ni@ACC interlayer achieve an ultra-high areal capacity of 4.05 mAh cm^{-2} at 1 C and demonstrate exceptional cycling stability over 12,000 cycles at 20 C. This work presents a facile and scalable method to synthesize highly efficient interlayers, advancing the development of high-performance Zn-I_2 batteries.

Results and discussion

Ultrafine Fe-Ni alloy nanoparticle catalysts uniformly dispersed on activated carbon cloth (ACC) fibers were synthesized using a two-step method incorporating Joule heating UHT treatment technology. Typically, the activated carbon cloth was pretreated with hydrochloric acid to improve the hydrophilicity and used as the substrate to absorb Fe^{3+} and Ni^{2+} cations in ethanol solvent (Figure S1). During the UHT process, the temperature rapidly increased to approximately 1550 K within just 1.4 s (Figure S2), achieving an ultrafast heating rate of ~1107 K s^{-1}, significantly higher than conventional tube furnace heating in the laboratory ($<$15 K·min^{-1}). Before Fe-Ni nanoalloys could aggregate into larger particles, the rapid cooling suppressed particle growth, ensuring the formation of ultrafine Fe-Ni alloy nanoparticle catalysts (~25 nm, Figure 1c) on the ACC, denoted as Fe-Ni@ACC. Notably, the UHT treatment not only facilitates the uniform dispersion of Fe-Ni alloy nanoparticles but also induces the formation of abundant nanocavities (Figure 1d). And these Fe-Ni alloy nanoparticles are found to be embedded and encapsulated within nanocavities (Figure 1e), resembling lotus seeds enclosed in a seedpod. The lotus seedpod-like reaction chambers provide strong binding interactions and facilitate efficient electron transfer between nanoparticle catalysts and carbon host, effectively accommodating iodine species diffusing from the electrode into the bulk electrolyte. The EDS mapping images (Figure 1f) illustrate a homogeneous dispersion of Fe and Ni elements within the nanoparticles, with an estimated Fe-Ni content of ~5 atom% on ACC (Figure S3). In contrast, the control sample heating in a conventional tube furnace with a slow heating rate leads to obvious diffusion and aggregation, resulting in the formation of larger alloy particles ($>$200 nm) with an exposed structure morphology on the ACC (Figure S4).

The X-ray diffraction (XRD) pattern of Fe-Ni@ACC (Figure 1g) exhibits characteristic peaks corresponding to both carbon substrate and Fe-Ni alloy (JCPDS No. 47-1417). Additionally, inductively coupled plasma (ICP) analysis determines the atomic ratio of Fe to Ni to be approximately 1.1:1. Raman spectroscopy analysis show that Fe-Ni@ACC has a higher I_D/I_G ratio (0.90) compared to Pristine ACC, indicating an increased amount of defects and edge sites after the UHT treatment (Figure 1h). N_2 adsorption/desorption curves and pore size distribution analyses (Figure 1i) reveal that both Fe-Ni@ACC and Pristine ACC exhibit typical Type IV isotherms, characteristic of predominantly microporous and mesoporous structures. Moreover, the UHT process induces the formation of more nanopore structures, increasing the Brunauer–Emmett–Teller (BET) surface area from 1077.1 m^2 g^{-1} to 1207 m^2 g^{-1} in Fe-Ni@ACC. This significant enhancement in surface area, coupled with a rich hierarchical porous architecture, provides ample space for catalytic conversion of iodine species and facilitates rapid charge transfer.

To further investigate the chemical state and local coordination environment of the Fe-Ni alloy nanoparticles at the atomic level, X-ray photoelectron spectroscopy (XPS) and extended X-ray absorption fine structure (EXAFS) spectroscopy were conducted. The XPS spectrum of Fe-Ni@ACC (Figure S5) confirm the presence of carbon (C), iron (Fe), and nickel (Ni). In the high-resolution Fe 2p spectrum (Figure 2a), small peaks at 707.3 eV and 720.4 eV indicate the presence of Fe (0). In the Ni 2p region (Figure 2b), two peaks at binding energies of 852.6 eV and 870.2 eV are observed, confirming the existence of Ni (0) species. The Fe K-edge X-ray absorption near-edge structure (XANES) of the Fe-Ni@ACC (Figure 2c) displays a pre-edge peak at 7114 eV, with absorption edge features resembling those of Fe foil. Similarly, the Ni K-edge XANES spectrum (Figure 2d) shows a pre-edge peak at 8335 eV and absorption edge characteristics similar to that of Ni foil. The Fourier-transformed EXAFS spectra reveal a Fe–Fe bond peak at 2.1 Å and a Ni–Ni bond peak at 2.05 Å, with no peaks observed for Fe–O or Ni–O, further confirming that the valence states of Fe and Ni in Fe-Ni@ACC are near zero, consistent with XPS results (Figure 2e-f). EXAFS data fitting analysis indicates a coordination number of 8.72 ± 0.64 for the Fe–Ni path in Fe and 7.04 ± 0.50 for the Ni–Fe path in Ni, suggesting the formation of a solid solution alloy, $Fe_{2.03}Ni_{1.97}$ (Figure S6 and Table S1). High-resolution wavelet transform (WT) plots (Figure 2g-l) reveal lobes at 2.12 Å and 8.02 $Å^{-1}$ in Fe foil, attributed to Fe–Fe contributions, while Ni foil exhibits lobes at 2.05 Å and 7.82 $Å^{-1}$, corresponding to Ni–Ni contributions. In contrast, the Fe-Ni@ACC exhibits distinct lobe structures at 2.08 Å and 8 $Å^{-1}$, which differ from Fe–O and Ni–O contributions and are attributed to Fe–Ni interactions, further confirming the formation of fine Fe-Ni solid solution alloy.

To further investigate the adsorption capacity for polyiodide, no interlayer (bare electrode), pristine ACC and Fe-Ni@ACC samples were separately immersed in a 4 mM $Zn(I_3)_2$ solution to observe the change. As shown in Figure 3a, the solution containing Fe-Ni@ACC became noticeably clearer, illustrating its superior adsorption ability. To further quantify the

View Article Online
DOI: 10.1039/D5EE01691F

adsorption capacity, ultraviolet-visible spectroscopy (UV-Vis) were recorded over time (Figures 3b-d). The characteristic peaks at 288 nm and 351 nm correspond to I_3^-. In the solution immersed with Fe-Ni@ACC, the I_3^- peaks are significantly diminished. Based on these results, it can be inferred that Pristine ACC may be insufficient to effectively absorbing polyiodide ions, especially under high mass load conditions. In contrast, the chemical adsorption feature of Fe-Ni nanoalloy, combined with the formation of lotus seedpod-like reaction chambers, strongly restricts polyiodide diffusion. To evaluate the electrochemical reaction kinetics, cyclic voltammetry (CV) measurements were performed on Zn-I_2 batteries with Fe-Ni@ACC and Pristine ACC interlayers were conducted at a scan rate of 0.2 mV s^{-1} (Figure3e). Both CV curves show a pair of redox peaks associated with the I_2/I^- oxidation-reduction reaction. Compared to Pristine ACC, the Fe-Ni@ACC shows higher peak currents and a smaller potential difference, indicating smaller polarization and improved reaction reversibility. Tafel slopes were calculated from linear sweep voltammetry (LSV) curves to further examine electrocatalytic activity. During the oxidation process, the Fe-Ni@ACC exhibits a Tafel slope of 180 mV dec^{-1}, lower than that of Pristine ACC (225 mV dec^{-1}). Similarly, in the reduction process (Figure 3g), the Tafel slopes for Fe-Ni@ACC and Pristine ACC are 228 mV dec^{-1} and 276 mV dec^{-1}, respectively, further demonstrating the superior electrocatalytic activity of Fe-Ni@ACC for I_2/I^- conversion.

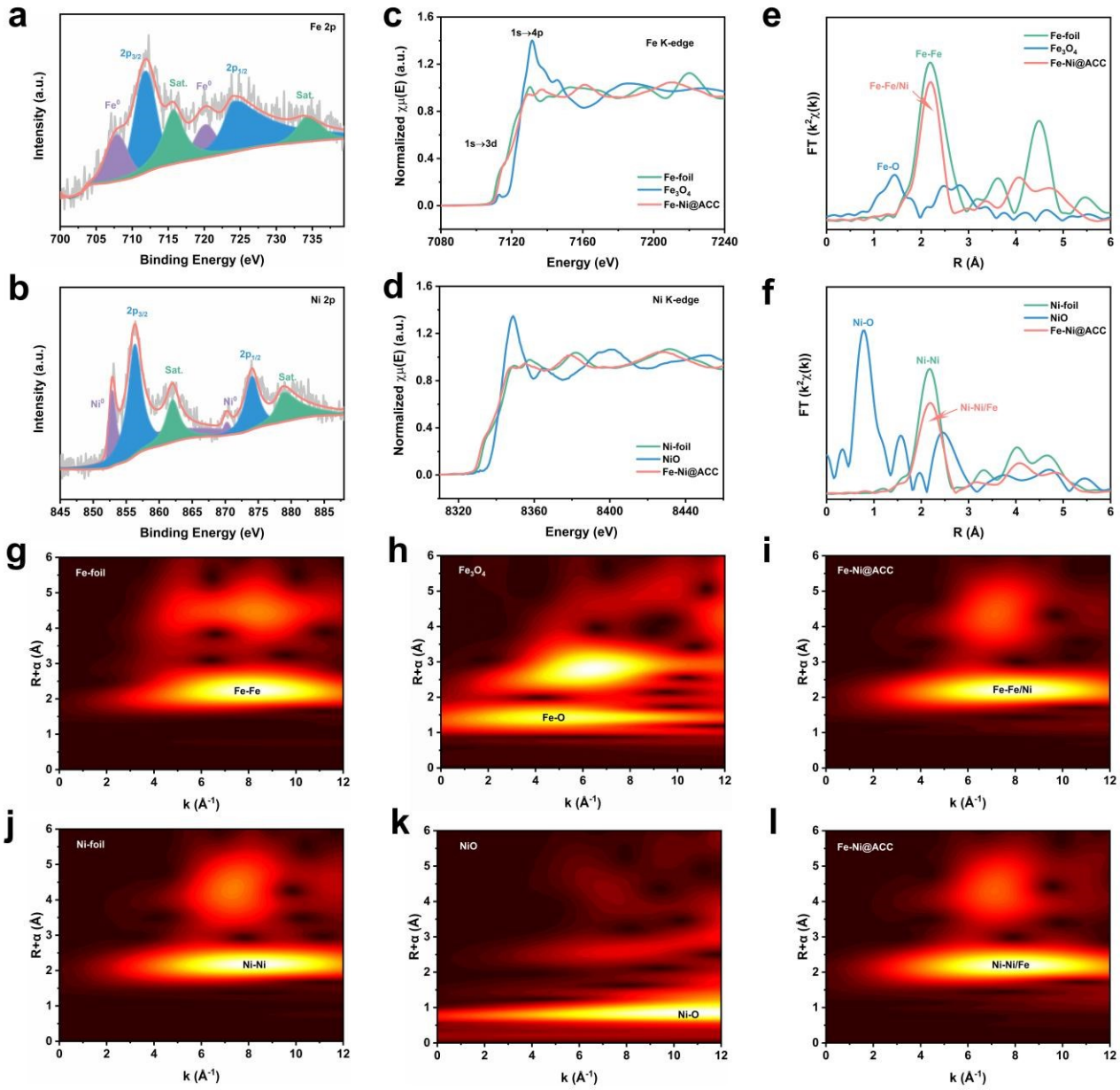

Fig. 2 (a) High-resolution XPS spectra of Fe 2p and (b) Ni 2p for Fe-Ni@ACC. (c) Normalized Fe K-edge and (d) Ni K-edge XANES spectra of Fe-Ni@ACC and reference samples. (e, f) FT of the EXAFS spectra in R-space for Fe-Ni@ACC. (g-l) WT-EXAFS plots of Fe-Ni@ACC.Figure caption.

View Article Online
DOI: 10.1039/D5EE01691E

Furthermore, the electrode reaction process is evaluated by analyzing the correlation between current (i) and scan rate(v)[39]

$i=av^b$

The b-values indicate the capacitive behavior predominates in both Fe-Ni@ACC and pristine ACC. (Figure. 3h and Figure. S8). To quantitatively differentiate the various current contributions, the capacitive contribution is determined using the following equation[40]

$i=k_1v+k_2v^{1/2}$

where k_1v and $k_2v^{1/2}$ represent current contributions from capacitive effects and diffusion-controlled processes, respectively. Fe-Ni@ACC exhibits enhanced capacitive contribution ratios of 66.2%, 72.1%, 74.8%, 80.8%, and 84.1% at scan rates of 0.1, 0.2, 0.3, 0.4, and 0.5 mV s^{-1} (Figure 3i and S9), surpassing those of pristine ACC (Figure S10). This capacitive dominance contributes to the superior high-rate capability of Fe-Ni@ACC.

The feasibility of the Fe-Ni@ACC interlayer was further evaluated through various electrochemical measurements of Zn-I_2 batteries. The self-discharge rate serves as a key metric determining battery storage performance, which is primarily influenced by polyiodide dissolution.

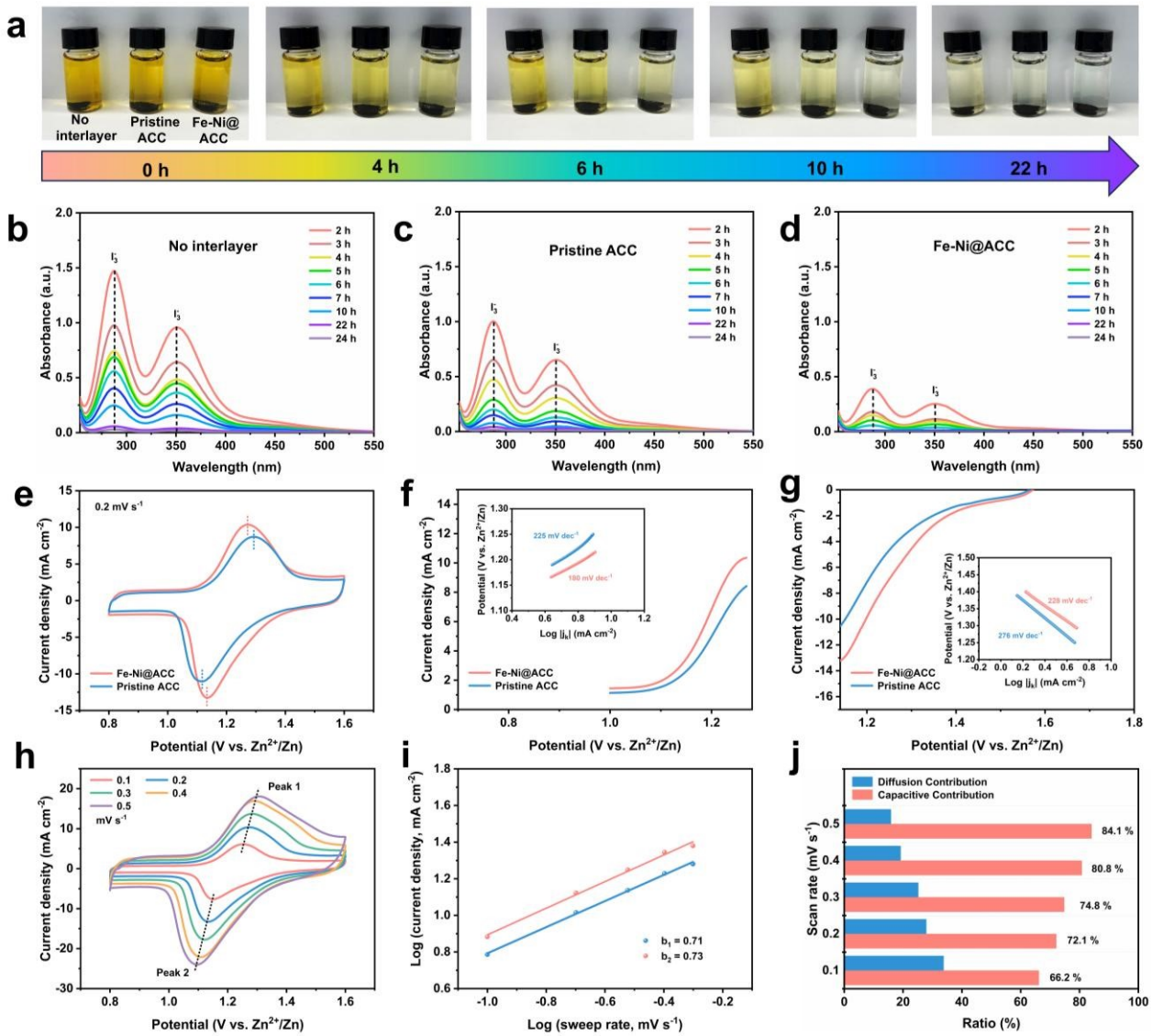

Fig. 3 (a) Digital photos for the solubility tests of No interlayer, Pristine ACC and Fe-Ni@ACC in $Zn(I_3)_2$ solution. (b-d) UV-Vis curves of 0.5 M $ZnSO_4$ in the upper layer of the serum bottle to determine the concentration of the I_3^- with (b) No interlayer, (c) Pristine ACC and (d) Fe-Ni@ACC. (e) CV curves of Fe-Ni@ACC and Pristine ACC interlayers at 0.2 mV s^{-1}. (f, g) LSV curves for the (f) oxidation and (g) reduction processes and the corresponding calculated Tafel slopes. (h) CV curves of the Fe-Ni@ACC interlayer at different scan rates. (i) Log i versus log v plots of the cathodic and anodic current response at the two peaks shown in CV curves of Figure 3h. (j) Estimated capacitive contributions at scan rates of 0.1, 0.2, 0.3, 0.4 and 0.5 mV s^{-1}.

View Article Online
DOI: 10.1039/D5EE01601E

As depicted in Figure 4a-c, after remaining fully charged for 48 hours, the Zn-I_2 battery with Fe-Ni@ACC still maintained a high capacity retention of 94.19%, outperforming those with Pristine ACC (90.78%) and No interlayer (81.51%), highlighting the superior physicochemical constraints provided by Fe-Ni@ACC in anchoring iodine species. EIS measurements were conducted to compare the charge-transfer processes. As shown in Figure 4d, the R_{ct} of the Zn-I_2 battery with Fe-Ni@ACC (40.1 Ω) was lower than that of the battery with the Pristine ACC (65.57 Ω), indicating more favorable charge transfer kinetics. Based on the temperature dependence of the charge transfer resistance, the activation energy (E_a) was calculated using the Arrhenius equation: $1/R_{ct} = Aexp(-E_a/RT)$.[41–43] The calculated E_a values for Fe-Ni@ACC and Pristine ACC were 35.08 kJ mol^{-1} and 55.09 kJ mol^{-1}, respectively, indicating that Fe-Ni@ACC significantly improves the reaction dynamics of iodine electrocatalysis (Figure 4e). As expected, the Zn-I_2 battery with Fe-Ni@ACC demonstrated superior rate performance compared to those with Pristine ACC or No interlayer (Figure 4f). At current densities of 1, 2, 5, 10, 15, and 20 C, the areal capacities were 4.05, 3.80, 3.36, 2.79, 2.35, and 1.97 mAh cm^{-2}, respectively. When the current density was returned to 1 C, the areal capacity fully recovered to 4.05 mAh cm^{-2}, demonstrating excellent rate capability. Although the addition of interlayer increases the total thickness (Table S2), the Zn-I_2 batteries assembled with the Fe-Ni@ACC interlayer still exhibits the highest volumetric energy density of 28.63 Wh L^{-1} due to the enhanced reversible areal capacity.

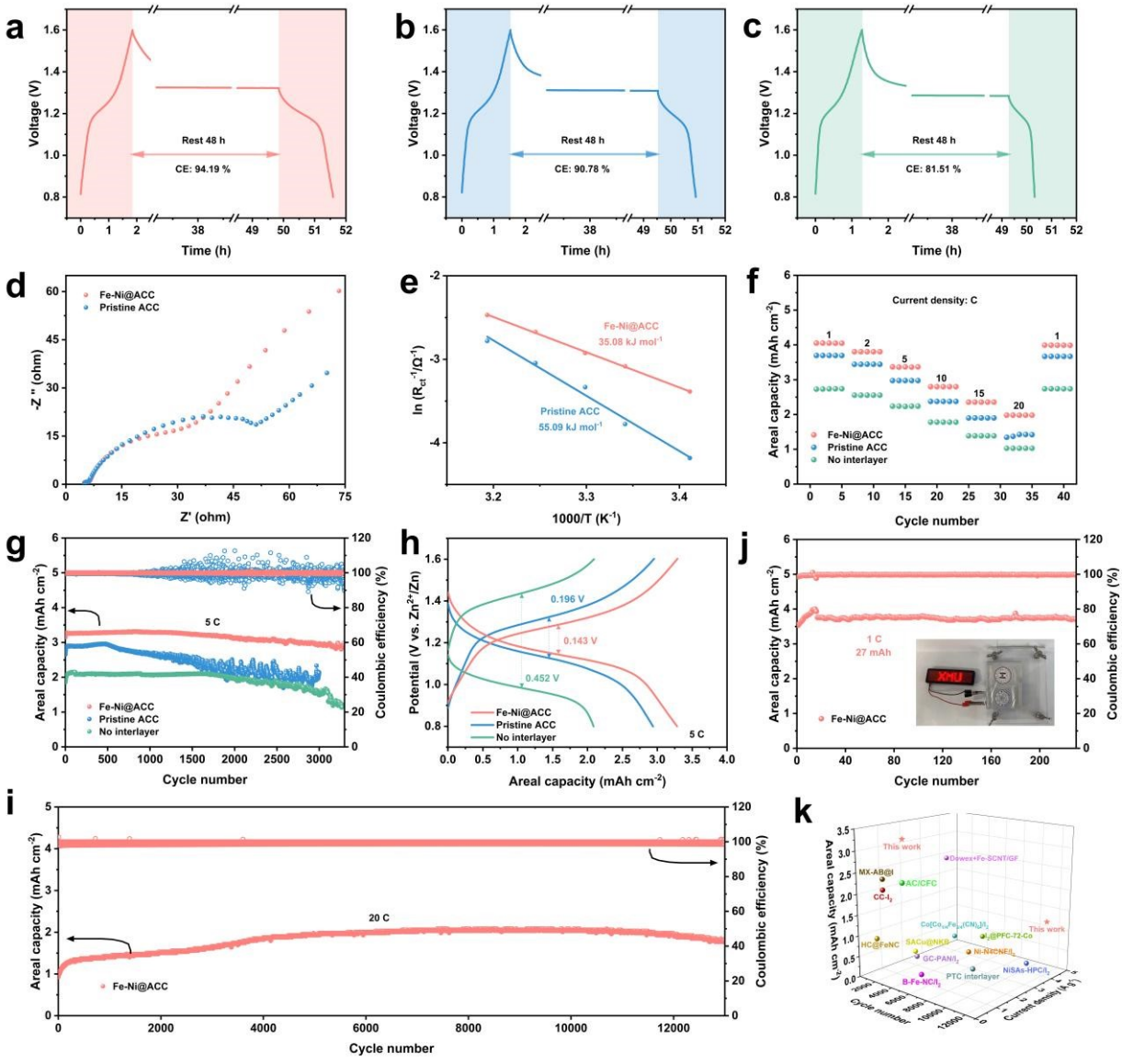

Fig. 4 Electrochemical performance of Zn-I_2 batteries. Self-discharging voltage-time profiles with (a) Fe-Ni@ACC, (b) Pristine ACC and (c) No interlayer. (d) Nyquist plots of Fe-Ni@ACC and Pristine ACC. (e) Arrhenius plots. (f) Rate performance. (g) cyclic performance at 5 C. (h) Galvanostatic discharge/charge profiles. (i) The long-term cyclic performance and Coulombic efficiencies of Zn–I_2 batteries using a Fe-Ni@ACC at 20 C. (j) cyclic performance at 1 C of pouch cell with Fe-Ni@ACC. (k) Comparative analysis of battery performance with reported Zn-I_2 batteries.

View Article Online
DOI: 10.1039/D5EE01615

To evaluate cycling stability, Zn-I_2 batteries with different interlayers were tested at 5 C (Figure 4g). Compared to Pristine ACC, Fe-Ni@ACC exhibited higher areal capacity and superior cycling stability, maintaining a high Coulombic efficiency of over 99.7%. Furthermore, during the charge/discharge process, Fe-Ni@ACC exhibited a smaller electrochemical polarization of 0.143 V (compared to 0.196 V for Pristine ACC and 0.452 V for No interlayer), indicating favorable redox kinetics (Figure 4h). To further investigate the impact of the interlayer on Zn anode stability, Zn-I_2 batteries with Fe-Ni@ACC and Pristine ACC were disassembled after 500 cycles at 5 C for post-mortem analysis (Figure S11-12). The Zn anode paired with Fe-Ni@ACC displayed a relatively smooth surface, fewer by-products, and a higher ratio of the 002 peak to the 101 peak, which indicated that zinc preferentially deposited on the (002) crystal plane.However, the anode in the Pristine ACC system exhibited a rough, corroded morphology. This significant difference suggests that the Fe-Ni@ACC, serving as a beneficial trapping material, aids in mitigating the shuttle phenomenon and corrosion reactions of I_3^-/I_5^- species and enable more uniform zinc deposition. Long-term cycling performance at high rates was further assessed (Figure S13). At a current density of 10 C and 15 C, the Zn-I_2 batteries with Fe-Ni@ACC exhibited an areal capacity of 2.8 and 2.5 mAh·cm^{-2} and significantly improved cycling stability. Importantly, under an ultra-high current density of 20 C, the Zn-I_2 battery with Fe-Ni@ACC also achieves an areal capacity of 2 mAh cm^{-2} and an exceptional cycling lifespan exceeding 12,000 cycles (Figure 4i). The promising application potential was demonstrated by fabricating pouch cell, which can successfully power light-emitting diodes (LEDs, 2.2 V), and a toy fan (Figure S14). Furthermore, the assembled pouch cell with a high areal capacity of 3.7 mAh cm^{-2} can maintain stable cycling over 200 cycles at 1 C (Figure 4j). Compared to the previously reported Zn-I_2 batteries (Table S3), the Fe-Ni@ACC interlayer significantly enhances areal capacity, cycle life, and rate capability, as illustrated in Figure 4k.[24,25,27,29,31,44–51]

To further investigate polyiodide evolution during electrochemical cycling, an in situ UV-Vis investigation was conducted using a quartz electrochemical chamber (Figure 5a). During the discharge process of Zn-I_2 battery with Pristine ACC, strong UV absorption signals corresponding to I_3^- were observed at 288 nm and 350 nm (Figure 5b).

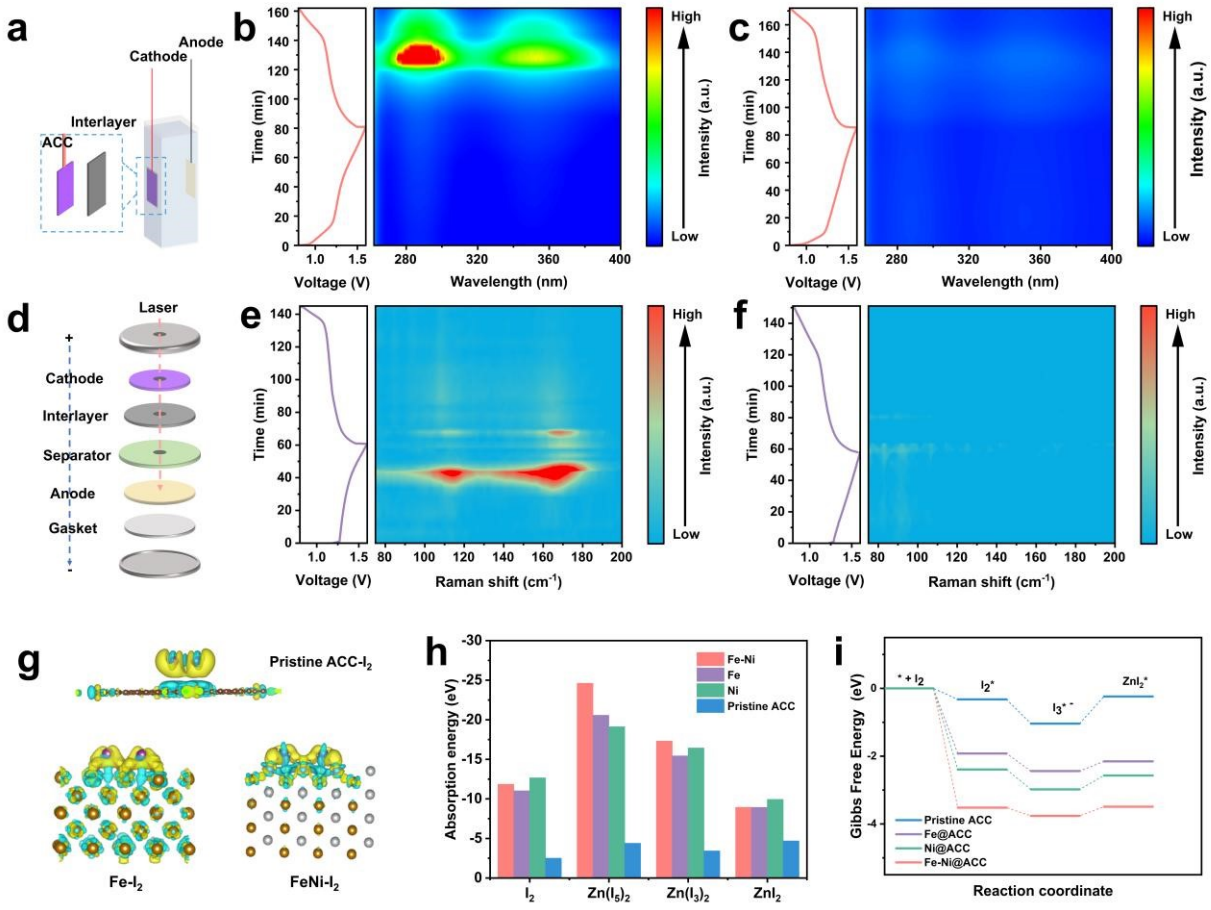

Fig. 5 The diagram of electrochemical cell device for in-situ (a) UV-Vis and (d) Raman. (b, c) In-situ UV–Vis spectra. (e, f) In-situ Raman spectrum of the I_3^- during the charge–discharge process with (e) Pristine ACC, and (f) Fe-Ni@ACC. (g) The charge differential density of that I_2 adsorbed on the surface of Pristine ACC, Fe metal and Fe-Ni alloy, respectively. (h) The energies of that I_2, $Zn(I_5)_2$, $Zn(I_3)_2$, and ZnI_2 adsorbed on the surface of Fe-Ni alloy, Fe metal, Ni metal and Pristine ACC. (i) Gibbs free energy diagram of I^- oxidation on Pristine ACC, Fe metal, Ni metal and Fe-Ni alloy.

In contrast, no detectable I_3^- signals were observed at these wavelengths in the Fe-Ni@ACC-based Zn-I_2 battery, suggesting efficient polyiodide conversion and suppression of the shuttle effect (Figure 5c).Additionally, in situ Raman spectroscopy (Figure 5d) was utilized to analyze the potential-dependent behavior of polyiodides and track their redox transitions. The signals at 110 and 163 cm^{-1} correspond to I_3^- and I_5^-, respectively (Figure 5e). During charging, the signal strengths of I_3^- and I_5^- gradually increased, while during discharge, these peaks decreased as the applied voltage decreased, suggesting the stepwise conversion from $I_5^- \rightarrow I_3^- \rightarrow I^-$. Notably, in the Pristine ACC-based Zn-I_2 battery, these peaks persisted until a discharge voltage of 0.8 V, suggesting weak polyiodide adsorption and incomplete conversion during cycling. In contrast, the Zn-I_2 battery using the Fe-Ni@ACC interlayer exhibited negligible I_3^- and I_5^- peaks throughout the charge-discharge process (Figure 5f), confirming that the Fe-Ni@ACC interlayer effectively adsorbs polyiodides and accelerates iodine redox conversion. In addition, comparable inferences can be derived from the high-resolution I 3d XPS spectra measured at both fully discharged and charged conditions (Figure S15) For the Pristine ACC interlayer, after charging to 1.6 V, most I^- in the electrolyte became I_2, which then combined with remaining I^- to form I_3^-. In the discharged state, I_3^- dominated, showing continuous reactions that dissolved active iodine and accumulated I_3^-. For the Fe-Ni@ACC interlayer, the fully charged I 3d spectrum showed I_3^-/I_2, while the discharged state featured mainly I^-. Significantly, Fe-Ni@ACC had far less residual I_3^- than Pristine ACC.

Additionally, the adsorption and catalytic mechanisms of Fe-Ni@ACC were investigated through density functional theory (DFT) calculations. The charge differential density plots of iodine on pristine CC, Fe metal, and Fe-Ni alloy surfaces were calculated, along with the adsorption of polyiodides on different substrates (Figure 5g, Figure S16-19). The structural changes in I_3^- and I_5^-, with noticeable elongation of I–I bonds, indicating a higher tendency for their reduction to I^-. As shown in Figure 5h, Fe-Ni alloy exhibit stronger adsorption energy for I_2, $Zn(I_5)_2$ and $Zn(I_3)_2$ compared to Pristine ACC and Fe metal. This enhanced adsorption facilitates I–I bond cleavage, thereby accelerating the I_2/I^- redox kinetics. Furthermore, the greater the degree of hybridization between the d orbitals of metal atoms and the p orbitals of iodine atoms, the more readily iodine species could be adsorbed.Compared to Fe and Ni metals, Fe-Ni alloy demonstrates greater overlap from the d orbitals of Fe-Ni alloy to the p orbitals of iodine, promoting efficient d–p hybridization (Figure S20). In addition to this orbital interaction, the position of the d-band center is also an important factor in determining the metal's conductivity and catalytic performance. As shown in Figure S21, the Fe-Ni alloy has a d-band center closest to the Fermi level (0.11 eV), showing superior catalytic activity. This signified that the Fe-Ni alloy had a stronger adsorption capacity for iodine monomers and relatively the best catalytic activity. To further evaluate the catalytic role of Fe-Ni@ACC during the I_2 reduction reaction, the Gibbs free energy was calculated for different metals on graphene-like carbon host and Pristine ACC (Figure 5i). The complete reduction process can be outlined below: $I_2 \rightarrow I_2^* \rightarrow Zn(I_3)_2^* \rightarrow ZnI_2^*$, where I_2^* and I_3^* are key intermediates. The more negative Gibbs free energy of Fe-Ni@ACC for the overall reaction ($I_2 \rightarrow ZnI_2^*$) suggests a thermodynamically favorable process in the presence of Fe-Ni alloy. Moreover, the rate-determining step, identified as $I_3^- \rightarrow I^-$, exhibits the lowest energy barrier when catalyzed by Fe-Ni alloy (0.27 eV), which is smaller than the energy barriers of Fe@ACC (0.28 eV), Ni@ACC (0.41 eV) and 0.81 eV for Pristine ACC, further confirming its superior catalytic activity in accelerating iodine redox kinetics. Fe-Ni@ACC has high affinity for polyiodides, a lower d-band energy gap value and a reduced ΔG value in the rate-limiting step, offering significant improvements in electrochemical performance and cycling stability.

Conclusions

In summary, this study successfully synthesized a biomimetic Fe-Ni@ACC interlayer via UHT treatment. Comprehensive in situ and ex situ characterizations reveal that the Fe-Ni@ACC effectively mitigates polyiodide shuttling and enhances the electrocatalytic redox transformation of iodine species. Fe-Ni@ACC facilitates highly efficient d-p orbital interaction, resulting in stronger binding of polyiodides and accelerating redox kinetics. Computational analysis further confirms that Fe-Ni@ACC exhibits the stronger adsorption capacity for polyiodides and the lower ΔG value in the determination step ($I_3^- \rightarrow I^-$ transition). Consequently, the Zn-I_2 batteries equipped with the Fe-Ni@ACC exhibit impressive electrochemical performance, achieving a high areal capacity of 4.05 mAh cm^{-2} at a current density of 1 C and over 12,000 cycles at 20 C. These results suggest that the Fe-Ni@ACC interlayer not only enhances the stability and efficiency of Zn-I_2 batteries but also opens up new opportunities for advancing high-efficiency energy storage devices utilizing polyiodide electrochemistry.

Author contributions

Conceptualization: R. T, J. Z and Y. Y. Experimental design and investigation: R. T. Data analyses: R. T, J. Y, S. L, W. M, M. Z, G. C, J. Z, and Y. Y. Calculation: C. S. Writing-original draft: R. T. Writing-review & editing: R. T, J. Z, and Y. Y.

Conflicts of interest

There are no conflicts to declare.

Data availability

The data that support the findings of this study are available from the corresponding author upon reasonable request.

Acknowledgements

The authors gratefully acknowledge the financial support from National Natural Science Foundation of China (No. 22379125,

22109030, and 22021001), Fundamental Research Funds for the Central Universities (20720220073), Fujian Industrial Technology Development and Application Plan (2022I0002), Key Research and Development Program Project of the Xinjiang Autonomous Region (2023B01025-1). The authors acknowledge Tan Kah Kee Innovation Laboratory for the help of scientific tests. The numerical calculations in this paper have been done on Hefei advanced computing center.

Notes and references

1 G. Zampardi and F. La Mantia, *Nat. Commun.*, 2022, **13**, 687.
2 Y. Zhao, P. Zhang, J. Liang, X. Xia, L. Ren, L. Song, W. Liu and X. Sun, *Advanced Materials*, 2022, **34**, 2204320.
3 N. Zhang, Y. Dong, M. Jia, X. Bian, Y. Wang, M. Qiu, J. Xu, Y. Liu, L. Jiao and F. Cheng, *ACS Energy Lett.*, 2018, **3**, 1366–1372.
4 N. Zhang, M. Jia, Y. Dong, Y. Wang, J. Xu, Y. Liu, L. Jiao and F. Cheng, *Adv. Funct. Mater.*, 2019, **29**, 1807331.
5 D. Zhao, Z. Li, D. Xu and Z. Yang, *Adv. Funct. Mater.*, 2024, **34**, 2316182.
6 Y. Zhao, Y. Huang, R. Chen, F. Wu and L. Li, *Mater. Horiz.*, 2021, **8**, 3124–3132.
7 H. Li, M. Cao, Z. Fu, Q. Ma, L. Zhang, R. Wang, F. Liang, T. Zhou and C. Zhang, *Chem. Sci.*, 2024, **15**, 4341–4348.
8 J. Ma, M. Wang, H. Zhang, L. Fu, W. Zhang, B. Song, S. Lu, Q. Chen and K. Lu, *Mater. Today Energy*, 2022, **30**, 101146.
9 J. Ma, M. Liu, Y. He and J. Zhang, *Angew. Chem., Int. Ed.*, 2021, **60**, 12636–12647.
10 S. Huang, R. Tang, X. Liu, Y. Zhang, Y. Tang, Z. Wen, M. Ye, Y. Yang and C. C. Li, *Energy Environ. Sci.*, 2024, **17**, 591–601.
11 C. Chen, Z. Li, Y. Xu, Y. An, L. Wu, Y. Sun, H. Liao, K. Zheng and X. Zhang, *ACS Sustainable Chem. Eng.*, 2021, **9**, 13268–13276.
12 J. Xu, Z. Huang, H. Zhou, G. He, Y. Zhao and H. Li, *Energy Storage Mater.*, 2024, **72**, 103596.
13 C. Xie, H. Zhang, W. Xu, W. Wang and X. Li, *Angew. Chem., Int. Ed.*, 2018, **57**, 11171–11176.
14 W. Yan, Y. Liu, J. Qiu, F. Tan, J. Liang, X. Cai, C. Dai, J. Zhao and Z. Lin, *Nat. Commun.*, 2024, **15**, 9702.
15 K. Li, S. Chen, S. Chen, X. Liu, W. Pan and J. Zhang, *Nano Res.*, 2019, **12**, 549–555.
16 Y. He, M. Liu, S. Chen and J. Zhang, *Sci. China Chem.*, 2022, **65**, 391–398.
17 Y. He, M. Liu and J. Zhang, *Adv. Sustainable Syst*, 2020, **4**, 2000138.
18 K. Li, B. Lin, Q. Li, H. Wang, S. Zhang and C. Deng, *ACS Appl. Mater. Interfaces*, 2017, **9**, 20508–20518.
19 Y. Li, H. Jia, U. Ali, B. Liu, L. Li, L. Zhang, H. Wang, T. Wang and C. Wang, *Chem. Eng. J.*, 2024, **483**, 149320.
20 L. Zhu, X. Guan, Z. Zhang, Z. Yuan, C. Zhang, Y. Wang, R. Xue, E. L. H. Mayes, Z. Yong, H. Xu, X. Li, H. Li, B. Jia, H. Yu, T. Ma and Y. Sun, *Small*, 2025, **21**, 2500223.
21 Z. Chen, F. Wang, R. Ma, W. Jiao, D. Li, A. Du, Z. Yan, T. Yin, X. Yin, Q. Li, X. Zhang, N. Yang, Z. Zhou, Q.-H. Yang and C. Yang, *ACS Energy Lett.*, 2024, **9**, 2858–2866.
22 Y. Zhang, U. Ali, Y. Hao, Y. Li, Y. Li, H. Jia, X. Liu and B. Liu, *J. Colloid Interface Sci.*, 2025, **688**, 132–139.
23 P. Hei, Y. Sai, W. Li, J. Meng, Y. Lin, X. Sun, J. Wang, Y. Song and X. Liu, *Angew. Chem., Int. Ed.*, 2024, **63**, e202410848.
24 Y. Wang, X. Jin, J. Xiong, Q. Zhu, Q. Li, R. Wang, J. Li, Y. Fan, Y. Zhao and X. Sun, *Advanced Materials*, 2024, **36**, 2404093.
25 M. Liu, Q. Chen, X. Cao, D. Tan, J. Ma and J. Zhang, *J. Am. Chem. Soc.*, 2022, **144**, 21683–21691.
26 C. Dong, Y. Yu, C. Ma, C. Zhou, J. Wang, J. Gu, J. Ji, S. Yang, Z. Liu, X. Xu and L. Mai, *Energy Environ. Sci.*, 2025, **18**, 3014–3025.
27 C. Guo, Y. Cao, Y. Gao, C. Zhi, Y. Wang, Y. Luo, X. Yang and X. Luo, *Adv. Funct. Mater.*, 2024, **34**, 2314189.
28 S. Chen, J. Ma, Q. Chen, W. Shang, J. Liu and J. Zhang, *Sci. Bull.*, 2025, **70**, 546–555.
29 L. Ma, G. Zhu, Z. Wang, A. Zhu, K. Wu, B. Peng, J. Xu, D. Wang and Z. Jin, *Nano Lett.*, 2023, **23**, 5272–5280.
30 L. Pei, D. Xu, Y. Luo, S. Guo, D. Liu, S. Jiang, W. Zhang and F. Cao, *Advanced Materials*, 2025, **37**, 2420005.
31 F. Yang, J. Long, J. A. Yuwono, H. Fei, Y. Fan, P. Li, J. Zou, J. Hao, S. Liu, G. Liang, Y. Lyu, X. Zheng, S. Zhao, K. Davey and Z. Guo, *Energy Environ. Sci.*, 2023, **16**, 4630–4640.
32 J. Yang, Y. Kang, F. Meng, W. Meng, G. Chen, M. Zhang, Z. Lv, Z. Wen, C. C. Li, J. Zhao and Y. Yang, *Energy Environ. Sci.*, 2025, **18**, 236–245.
33 H. Ou, D. Wang and Y. Li, *Nano Sel.*, 2021, **2**, 492–511.
34 H. Li, X. Shu, P. Tong, J. Zhang, P. An, Z. Lv, H. Tian, J. Zhang and H. Xia, *Small*, 2021, **17**, 2102002.
35 L. Zhu, X. Guan, Y. Fu, Z. Zhang, Y. Li, Q. Mai, C. Zhang, Z. Yuan, Y. Wang, P. Li, H. Li, D. Su, B. Jia, H. Yu, Y. Sun and T. Ma, *Adv. Funct. Mater.*, 2024, **34**, 2409099.
36 Y. Li, H. Jia, Y. Hao, U. Ali, B. Liu, L. Zhang, L. Li, R. Lian and C. Wang, *Adv. Funct. Mater.*, 2025, 2419821.
37 W. Huang, Z. Lian, R. Zou, Q. Wang, U. Feleni, E. I. Iwuoha, X. Peng and L. Zhong, *ACS Appl. Nano Mater.*, 2025, **8**, 1991–1999.
38 Y. Gao, Y. Liu, X. Guo, J. Zhang, C. Zhou, F. Li, Z. Xu, Z. Zhao, Z. Xing, P. Rao, Z. Kang, X. Tian and X. Shi, *Adv. Funct. Mater.*, 2024, **35**, 2421714.
39 H. Lindström, S. Södergren, A. Solbrand, H. Rensmo, J. Hjelm, A. Hagfeldt and S.-E. Lindquist, *J. Phys. Chem. B*, 1997, **101**, 7717–7722.
40 V. Augustyn, P. Simon and B. Dunn, *Energy Environ. Sci.*, 2014, **7**, 1597.
41 Z. Deng, Z. Zhang, Y. Lai, J. Liu, J. Li and Y. Liu, *J. Electrochem. Soc.*, 2013, **160**, A553–A558.
42 R. Lei, Y. Yang, C. Yu, Y. Xu, Y. Li and J. Li, *Sustainable Energy Fuels*, 2021, **5**, 1538–1547.
43 L. Peng, Z. Wei, C. Wan, J. Li, Z. Chen, D. Zhu, D. Baumann, H. Liu, C. S. Allen, X. Xu, A. I. Kirkland, I. Shakir, Z. Almutairi, S. Tolbert, B. Dunn, Y. Huang, P. Sautet and X. Duan, *Nat Catal*, 2020, **3**, 762–770.
44 L. Zhang, M. Zhang, H. Guo, Z. Tian, L. Ge, G. He, J. Huang, J. Wang, T. Liu, I. P. Parkin and F. Lai, *Adv. Sci.*, 2022, **9**, 2105598.
45 L. Ma, Y. Ying, S. Chen, Z. Huang, X. Li, H. Huang and C. Zhi, *Angew. Chem., Int. Ed.*, 2021, **133**, 3835–3842.
46 W. Qu, J. Zhu, G. Cao, S. Chen, Y. Tan, B. Chen and M. Zhang, *Small*, 2024, **20**, 2310475.
47 Y. Zhang, T. Zhao, S. Yang, Y. Zhang, Y. Ma and Z. Wang, *J. Energy Chem.*, 2022, **75**, 310–320.
48 S. Lv, T. Fang, Z. Ding, Y. Wang, H. Jiang, C. Wei, D. Zhou, X. Tang and X. Liu, *ACS Nano*, 2022, **16**, 20389–20399.
49 Y. Kang, G. Chen, H. Hua, M. Zhang, J. Yang, P. Lin, H. Yang, Z. Lv, Q. Wu, J. Zhao and Y. Yang, *Angew. Chem., Int. Ed.*, 2023, **62**, e202300418.
50 Y. Yang, S. Liang, B. Lu and J. Zhou, *Energy Environ. Sci.*, 2022, **15**, 1192–1200.
51 D. Li, Y. Zhu, L. Cheng, S. Xie, H. Yu, W. Zhang, Z. Xu, M. Ma and H. Li, *Adv. Energy Mater.*, 2024, 2404426.

View Article Online
DOI: 10.1039/D5EE01691F

Data availability

The data that support the findings of this study are available from the corresponding author upon reasonable request.